where these quantities should be larger than at $P > P_m$, away from the stability region of the liquid. It is also possible that the superfluid transition temperature T_c^{GB} is considerably lower than 1 K at high P, where superfluidity may concern only a fraction of a monolayer. Unfortunately, to work with a single GB while varying the temperature and P is not easy. One should also study the effect of ^{3}He impurities because these should adsorb on GBs and modify their superfluid properties.

Let us finally consider the values of ρ_s and v_c found in torsional oscillator experiments (*1*–*5*). If the superflow occurs along the GBs in these experiments as well, v_c needs to decrease sharply from meters per second at P_m to micrometers per second above P_m. This is possible if the thickness of GBs also decreases as a function of P. A 1% superfluid density can be achieved with one GB every 100 *e*. We have found that, when growing crystals above 1.8 K from normal liquid helium, as is usually the case when using the blocked capillary method of KC and others, the growth is dendritic and the solid sample is snowball-like, in which the density of defects is so large that it strongly scatters light [see photograph in (*5*)]. It is also possible that KC's experiment is insensitive to annealing because GBs are more strongly pinned in their cell. If GBs are close to each other, elastic interactions might couple them and mimic phase coherence. As a final note, we mention that KC observed that $\rho_s(P)$ increases up to 55 bars before decreasing at higher P. The increase could be due to an increasing number of GBs and the decrease to the vanishing of superfluidity around 200 bars (*29*).

References and Notes

1. E. Kim, M. H. W. Chan, *Nature* **427**, 225 (2004).
2. E. Kim, M. H. W. Chan, *Science* **305**, 1941 (2004).
3. A. S. C. Rittner, J. D. Reppy, published online 22 April 2006 (http://arxiv.org/PS_cache/cond-mat/pdf/0604/0604528.pdf).
4. K. Shirahama, M. Kondo, S. Takada, Y. Shibayama, American Physical Society, Baltimore, MD, 14 March 2006 (abstract G41.00007).
5. A. Cho, *Science* **311**, 1693 (2006).
6. E. Burovski, E. Kozik, A. Kuklov, N. Prokof'ev, B. Svistunov, *Phys. Rev. Lett.* **94**, 165301 (2005).
7. A. F. Andreev, I. M. Lifshitz, *Sov. Phys. JETP* **29**, 1107 (1969).
8. G. V. Chester, *Phys. Rev. A.* **2**, 256 (1970).
9. A. J. Leggett, *Phys. Rev. Lett.* **25**, 1543 (1970).
10. D. E. Galli, L. Reatto, *Phys. Rev. Lett.* **96**, 165301 (2006).
11. This is when KC used natural ^{4}He containing ≈0.1 parts per million of ^{3}He impurities. We used the same natural ^{4}He.
12. B. K. Clark, D. M. Ceperley, *Phys. Rev. Lett.* **96**, 105302 (2006).
13. M. Boninsegni, N. Prokof'ev, B. Svistunov, *Phys. Rev. Lett.* **96**, 105301 (2006).
14. G. Dash, J. S. Wettlaufer, *Phys. Rev. Lett.* **94**, 235301 (2005).
15. S. A. Khairallah, D. M. Ceperley, *Phys. Rev. Lett.* **95**, 185301 (2005).
16. P. W. Anderson, W. F. Brinkman, D. A. Huse, *Science* **310**, 1164 (2005).
17. J. Day, T. Herman, J. Beamish, *Phys. Rev. Lett.* **95**, 035301 (2005).
18. J. Day, J. Beamish, *Phys. Rev. Lett.* **96**, 105304 (2006).
19. Because of radiation through the windows, there is a small heat input inside the tube, but it is less than 1 μW. In principle, P_m inside the tube could thus be different from that outside and maintain an $h(t)$ between the two levels. However, given the heat conductivity of the solid (*20*) and the melting curve $P_m(T)$ (*21*), where T is temperature, one finds that the level difference is less than 3 μm below 0.5 K. We thus expect thermal effects to be unimportant and gravity to be the only relevant parameter governing the shape evolution.
20. B. Bertman, H. A. Fairbank, C. W. White, M. J. Crooks, *Phys. Rev.* **142**, 74 (1966).
21. H. N. Hanson, J. E. Berthold, G. M. Seidel, H. J. Maris, *Phys. Rev. B* **14**, 1911 (1976).
22. In liquid ^{4}He, a 1-cm difference in height induces a difference in P of 2×10^{-4} bars, which is very small compared to the Young modulus $E = 300$ bars of ^{4}He crystals (*23*). As a consequence, it cannot induce the large plastic deformation that would be necessary for the crystal to flow around the tube edge.
23. H. J. Maris, T. E. Huber, *J. Low Temp. Phys.* **48**, 99 (1982).
24. E. R. Grilly, *J. Low Temp. Phys.* **11**, 33 (1973).
25. S. Balibar, H. Alles, A. Y. Parshin, *Rev. Mod. Phys.* **77**, 317 (2005).
26. G. Bonfait, H. Godfrin, B. Castaing, *J. Phys. (Paris)* **50**, 1997 (1989).
27. K. Telschow, I. Rudnick, T. G. Wang, *Phys. Rev. Lett.* **32**, 1292 (1974).
28. K. A. Gillis, S. M. Volz, J. M. Mochel, *Phys. Rev. B* **40**, 6684 (1989).
29. R. Ishiguro, F. Caupin, S. Balibar, *Europhys. Lett.* **75**, 91 (2006).

30. We acknowledge support from Agence Nationale de la Recherche grant 05-BLAN-0084–01 and NSF grant DMR-0305115. R.I. acknowledges support from the Japan Society for the Promotion of Science for a Postdoctoral Fellowship for Research Abroad (April 2004 to March 2006).

5 June 2006; accepted 19 July 2006
Published online 27 July 2006;
10.1126/science.1130879
Include this information when citing this paper.

Detection, Stimulation, and Inhibition of Neuronal Signals with High-Density Nanowire Transistor Arrays

Fernando Patolsky,[1]* Brian P. Timko,[1]* Guihua Yu,[1] Ying Fang,[1] Andrew B. Greytak,[1] Gengfeng Zheng,[1] Charles M. Lieber[1,2]†

We report electrical properties of hybrid structures consisting of arrays of nanowire field-effect transistors integrated with the individual axons and dendrites of live mammalian neurons, where each nanoscale junction can be used for spatially resolved, highly sensitive detection, stimulation, and/or inhibition of neuronal signal propagation. Arrays of nanowire-neuron junctions enable simultaneous measurement of the rate, amplitude, and shape of signals propagating along individual axons and dendrites. The configuration of nanowire-axon junctions in arrays, as both inputs and outputs, makes possible controlled studies of partial to complete inhibition of signal propagation by both local electrical and chemical stimuli. In addition, nanowire-axon junction arrays were integrated and tested at a level of at least 50 "artificial synapses" per neuron.

Electrophysiological measurements made with micropipette electrodes and microfabricated electrode arrays play an important role in understanding signal propagation through individual neurons and neuronal networks (*1*–*5*). Micropipette electrodes can stimulate and record intracellular and extracellular potentials in vitro and in vivo with relatively good spatial resolution of ~100 nm per pipette and ≥10 μm between two pipettes (*2*, *6*–*8*), yet they are difficult to multiplex. Microfabricated structures, such as electrode and field-effect transistor (FET) arrays, have potential for large-scale multiplexing and have enabled recording from both individual neurons and networks (*3*–*5*, *9*–*14*). However, these structures have relatively large sizes (~10 μm and larger on edge), and their interelectrode spacing (>10 μm) has precluded detection and stimulation of neuronal activity at the level of individual axons and/or dendrites.

For a FET array to be used to stimulate, inhibit, and record neuronal signals from numerous locations along the neuronal projections and cell body, the gate dimensions should ideally be on the nanometer scale, and appropriate contact between the neuron and the array must be made. Silicon nanowire (SiNW) FETs (*15*) have been used to detect chemical and biological species (even single virus particles) in solution (*16*–*19*). We show that we can pattern arrays of SiNW FETs on a substrate and passivate the arrays such that they will function in cell-culture media. Polylysine patterning allowed us to direct the growth of rat neurons to ensure that numerous SiNW FET contacts were made to the same neuron, rather than rely on fortuitous overlap. Because the contact length along an

[1]Department of Chemistry and Chemical Biology, [2]Division of Engineering and Applied Sciences, Harvard University, Cambridge, MA 02138, USA.

*These authors contributed equally to this work.
†To whom correspondence should be addressed. E-mail: cml@cmliris.harvard.edu

axon or dendrite projection crossing a NW is only on the order of 20 nm, these devices are highly local and noninvasive probes of neuronal projections. Notably, the typical active junction area for devices, about 0.01 to 0.02 μm^2, is three orders of magnitude smaller than microfabricated electrodes and planar FETs. The small hybrid junction sizes, which are similar to natural synapses, offer important advantages compared with other electrophysiological methods, including spatially resolved detection of signals without complications of averaging extracellular potential changes over a large percentage of a given neuron and integration of multiple elements on the axon and dendrite projections from a single neuron.

Our strategy for preparing SiNW-neuron devices involves assembly of oriented p- and/or n-type SiNWs (*18*, *20*, *21*), interconnection into FET device array structures (*18*, *22*), patterning polylysine as an adhesion and growth factor to define neuron cell growth (*23*, *24*) with respect to the device elements, and growing neurons under standard conditions (*25*). There are several features of the fabrication that are critical to the success of our approach. First, the metal-SiNW contacts must be passivated, because these readily corrode and fail during the relatively harsh conditions of cell culture and subsequent measurement. We developed a simple yet reliable single-step lithography process using an undercut multilayer resist and sequential line-of-sight metal and isotropic silicon nitride passivation layer depositions. Devices prepared in this manner survived continuous cell-culture conditions at 37°C for at least 10 days with >90% yield.

Second, we achieved a high yield of specific SiNW-neuron structures by using a second lithography step to pattern polylysine to define square regions 30 to 60 μm on edge that promote cell body adhesion and projected ~2-μm-wide lines that help to define subsequent neurite growth (Fig. 1A). Under growth conditions, cell suspensions were transferred to patterned chips for ~1 hour of incubation, washed to remove excess cells from regions other than polylysine pattern, and then incubated for an additional 4 to 8 days to allow for neuronal growth (*25*). This overall approach allowed us to vary the addressable NW interdevice separations down to at least 100 nm (*24*) and create a range of device array geometries that varied the number and spatial location of the SiNW junctions with respect to the cell body and neurite projections. We could also incorporate electronically distinct p- and n-type elements in well-defined positions.

Optical images of a representative one-neuron/one-NW device from an array (Fig. 1, B and C, and fig. S1) showed the expected 1:1 hybrid live-cell NW device with selective growth of the axon, verified by marker-specific fluorescence labeling and multicolor confocal microscopy (*25*). Analysis of this and additional chips indicates yields in excess of 90%, where clean patterning of polylysine and attachment of isolated live cells were critical factors.

We elicited action potential spikes using either a conventional glass microelectrode impaled at the soma or the SiNW-axon contact. In either case, we recorded the intracellular potential (IC) and conductance at the microelectrode and NW FET, respectively. All of the electrical experiments reported in this work were carried out at 37°C with chips submerged in electrophysiology bath solution (*26*), and stable NW measurements can be made for at least 24 hours. Figure 1D shows the direct temporal correlation between the potential spikes initiated in the soma and the corresponding conductance peaks measured by the SiNW at the NW-axon junction. Expanded plots of single peaks exhibit shapes characteristic of neuronal action potentials. The direct correlation of the NW conductance peak with intracellular (IC) potential peak is expected for a p-type NW (these devices), because the relative potential at the outer membrane becomes more negative and then more positive (opposite to the measured IC potential) and causes an accumulation of carriers (enhanced conductance) followed by a depletion of carriers (reduced conductance), respectively (*16*, *26*). Devices with n-type SiNWs [fig. S2 and supporting online material (SOM) text] showed signals that were negatively correlated. Moreover, the magnitude of the conductance change is consistent with estimates based on SiNW FET device properties and the range of axon diameters that form the NW-axon junctions (*25*).

Control experiments showed that IC stimulation with higher frequency action potential spikes resulted in correspondence between the potential spikes initiated in the soma and the conductance peaks measured by the NW (fig. S3). Also, no conductance spikes were detected after blocking voltage-dependent sodium channels with tetrodotoxin (TTX) (fig. S4A) (*8*, *27*), after severing the axon anterior to the NW-axon junction (fig. S4B), or when the SiNW element was absent in the same axon-electrode geometry (fig. S4C). In addition, NW-soma hybrid structures allow detection of signals at the soma (fig. S5).

NW devices were used to apply biphasic excitatory pulse sequences (Fig. 1E) to create detectable somatic action potential spikes in 86% of the trials, which is similar to the yield achieved with microelectrodes interfaced with entire cells (*14*). The stimulation process was carried out at least 30 times over a 4-hour period without loss of potential spikes or cell viability (fig. S6A) and thus shows that the excitation, which could involve reversible electroporation or capacitive coupling (*5*, *11*, *28*), does not damage the neurons. The excitation shows a threshold of about 0.4 V and no potential spikes in the presence of TTX or the absence of the SiNW (fig. S6B). In addition, single SiNWs can be used for simultaneous stimulation and detection (fig. S6C).

We next assembled hybrid structures that consisted of a central cell body and four peripheral SiNWs arranged at the corners of a rectangle; polylysine patterning promoted neu-

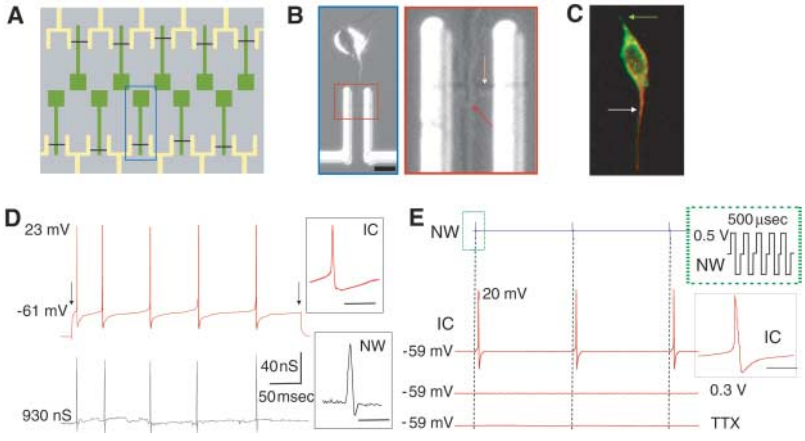

Fig. 1. NW recording and stimulation of neuronal axon signals. (**A**) General schematic of aligned NW-neuron device array. The open blue rectangle highlights a single NW-neuron device. (**B**) Optical image of a single cortex neuron aligned across a single NW device and (red box) a magnified image of the area where the axon crosses the NW. White arrow denotes the nanowire element; red arrow denotes the neuronal axon. (**C**) Confocal fluorescence image for a dual color–labeled cortex neuron after 4 days in culture. The red section (highlighted by the white arrow) highlights the growing axon, and the green short section (highlighted by the gray arrow) represents a dendrite. (**D**) (Top left) IC potential of an aligned cortex neuron (after 6 days in culture) during stimulation with a 500-ms-long current injection step of 0.1 nA. (Bottom left) Time-correlated signal from axon measured with a p-type silicon NW device. (**E**) Local NW-axon stimulation and correlated IC electrical recording of a cortex neuron. IC plots were recorded following a rectangular biphasic train of stimuli with amplitudes of (top) 0.5 V, (middle) 0.3 V, and (bottom) 0.5 V after bath application of 0.5 μM TTX. Green box highlights the train of rectangular biphasic voltage pulses.

rite growth across these elements. A representative optical image (Fig. 2A) shows one NW-axon and two NW-dendrite elements at positions 1, 2, and 3, respectively. Stimulation of action potential spikes in the soma yields correlated conductance peaks in the NW-axon (NW1) and NW-dendrite (NW2 and NW3) devices (Fig. 2B), but no signal was observed in a good detector (NW4) that had no visible neurite overlap.

This multi-NW–neurite array was then used to study spike propagation in the absence of the IC microelectrode with NW1 as a local input to elicit action potential spikes from the axon rather than the cell body. After stimulation with a biphasic pulse sequence (Fig. 2C), we detected back-propagation of the elicited action potential in the two dendrites crossing elements NW2 and NW3. The lack of observed signal from NW4 demonstrates the absence of cross-talk in the hybrid device array.

A linear array of four-NW FETs, a gap, and five-NW FETs was used to investigate simultaneous and temporally resolved propagation and back-propagation of action potential spikes in axons and dendrites, respectively. Optical images (Fig. 2D) revealed that the specific polarity of growth (e.g., axon across the four- or five-FET array) is not controlled but is readily identified by the faster growing projection (the axon) during culture and subsequently by electrical response and postmeasurement fluorescent imaging. On a given "chip," we fabricated ~20 of the repeating NW array structures, and after low-density neuron adsorption and growth, we obtained a yield of ~80% hybrid structures per chip. We then simultaneously detected the conductance output from NWs after IC stimulation at the soma and found that stimulation of action potential spikes in the soma yielded correlated conductance peaks in NW elements that form the NW-axon and NW-dendrite junctions (Fig. 2E).

These data demonstrate several key points. First, seven of the nine independently addressable NW-neurite junctions yield reproducible conductance spikes correlated with IC stimulation. Higher yields of functioning elements have also been achieved, although this ~80% yield still leaves three and four spatially defined local detectors on the dendrite and axon, respectively. While previous studies using glass microelectrodes have recorded spike propagation in axons and dendrites (*6*, *7*, *27*, *29*), axon and dendrite propagation has not been measured simultaneously, nor has the same level or recording points been achieved [although it has been demonstrated that measurements can be taken at multiple points by moving a single-pipette probe (*27*, *29*)].

Second, a comparison of high-resolution conductance-time data (Fig. 2F) demonstrates that the propagation delay of spikes in the dendrite and axon after initiation in the soma can be resolved, and moreover, shows a clear peak reduction and temporal spreading in the

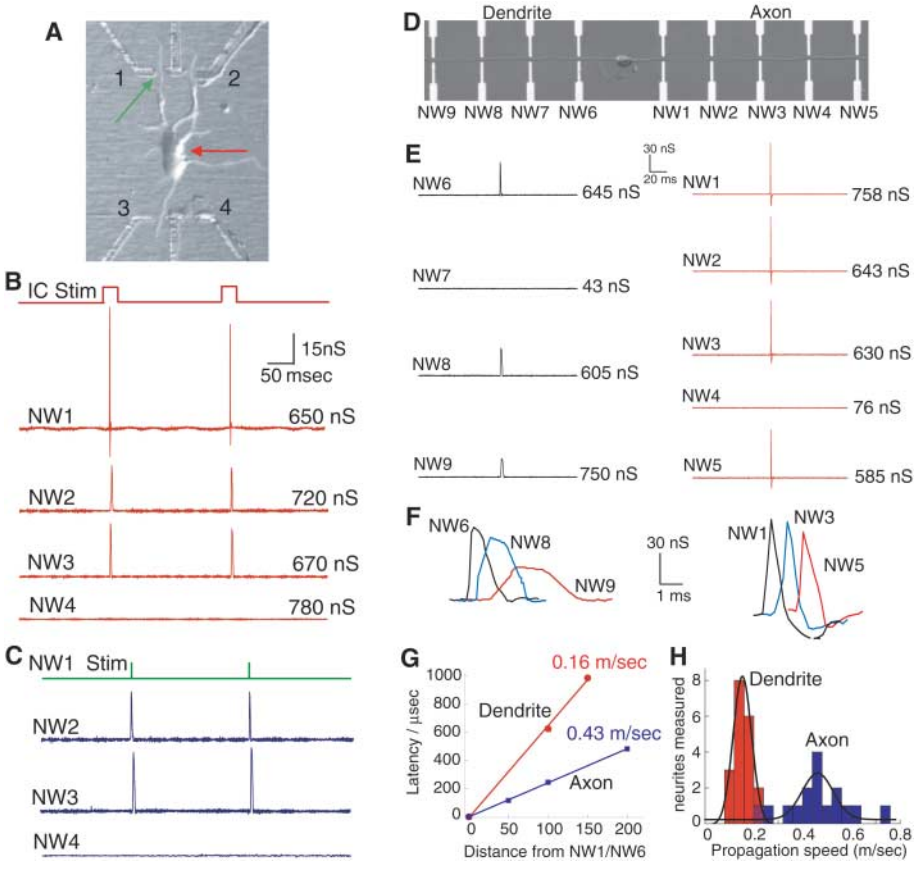

Fig. 2. Multi-NW–neurite structures. (**A**) Optical image of a cortex neuron connected to three of the four functional NW devices in the array. Two possible stimulation approaches are indicated: intracellular stimulation (red arrow in soma) and extracellular NW-based stimulation (green arrow on NW1). (**B**) Trace of intracellular current stimulation (15-ms current injection pulses of 0.5 nA) and resulting NW (NW1, NW2, NW3, and NW4) electrical responses. NW4 is not electrically connected to any section of the neuron and thus functions as an internal control for all the experiments. (**C**) Trace of pulses (trains of five rectangular biphasic-type stimuli, train width of 500 μs) applied to NW1 for antidromic stimulation of the neuron. The response was measured by the NW-dendrite junctions at NW2 and NW3. (**D**) Optical image of a cortex neuron with axon and dendrite aligned in opposite directions. (**E**) Electrical responses measured from NW-dendrite devices (left, NW6 to NW9) and NW-axon devices (right, NW1 to NW5) after intracellular stimulation with a 15-ms, 0.5-nA current pulse. (**F**) Expansion of peaks from (E) elucidating the evolution of peak shape as it propagates along each process. (**G**) Plot showing latency time as a function of distance from NW1 and NW6 for axons (blue) and dendrites (red), respectively. (**H**) Histogram of propagation speed through axons (blue) and dendrites (red).

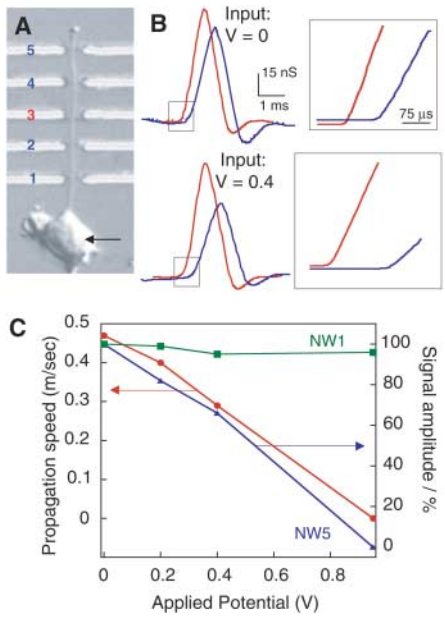

Fig. 3. Electrical modulation of signal propagation. (**A**) Optical image showing the structure of the five-NW–axon structure, where NW3 serves as input. (**B**) Electrical signals recorded at NW1 (red) and NW5 (blue) before (top) and after (bottom) IC stimulation; a bias (hyperpolarizing) of 0.4 V was applied to NW3. (**C**) Plot of spike propagation speed (red) and amplitude (green and blue) as a function of input potential applied to NW3, where signals were recorded at NW1 and NW5.

dendrite, measured by elements 6 to 9, and little change in the axon, recorded by elements 1 to 5. These latter observations are consistent with passive and active propagation mechanisms, respectively (*30*, *31*). By using the first NW (i.e., NW1 and NW6) in each neurite as references, we calculated (Fig. 2G) signal propagation rates of 0.16 m/s for dendrites and 0.43 m/s for axons. In trials with different neurons, we found these rates to have Gaussian distributions of 0.15 ± 0.04 (±SD) and 0.46 ± 0.06 m/s for dendrites and axons, respectively (Fig. 2H); these data are comparable to reported propagation rates measured by conventional electrophysiological (*32*) and optical (*33*–*35*) methods.

Hybrid structures consisting of five independent NW-axon elements (Fig. 3A) were fabricated and used to study the effects of local electrical and chemical inputs on signal propagation. We initially configured the middle NW-axon junction, NW3, as a variable potential input and used the other four NWs elements to record temporally resolved spike propagation after IC stimulation. A comparison of the time-resolved spikes recorded from NW1 and NW5 for input voltages of 0 and 0.4 V (Fig. 3B) shows that there is well-defined slowing of the propagation speed and reduction of the peak amplitude when V(NW3) = 0.4 V. Systematic inhibition and ultimately complete blocking of propagation was observed as the input voltage on NW3 is increased to 0.9 V (Fig. 3C). Indeed, if any one of the first four NW inputs is set at or above the blocking threshold of 0.9 V, no signal propagation is detected at NW5 (fig. S7). The spike amplitude recorded at NW5 was monotonically reduced with increasing input voltage, although no change is observed in the amplitude at NW1, which is equidistant from the input, NW3 (Fig. 3C). These results suggest that mode of action is localized at a given NW-axon input and is consistent with local anodic hyperpolarization of the membrane at NW-axon synapses. This polarization inhibits and ultimately blocks the propagation of action potential spikes (*36*, *37*). In a similar manner, the effects of local chemical inputs, such as TTX, on signal propagation were characterized (SOM text and fig. S8).

Our approach can be readily extended to highly integrated systems. We designed and fabricated a repeating structure that consists of 50 addressable NW-axon elements. This structure was chosen to show the capability of single-cell hybrid structures at much higher density of nanoelectronics devices but could be readily reconfigured, for example, into structures with different geometries, NW-device spacing, and/or multiple cells. An optical image (Fig. 4A) shows that well-aligned neuron growth was achieved. Electrical transport measurements made after neuron growth demonstrate a high yield of good NW FET devices: 43 out of 50 devices had conductance values from 550 to 870 nS. Notably, IC stimulation of action potentials in the soma yields a mapping of the spike propagation by the 43 working devices over the ~500-μm-long axon (Fig. 4B). These data exhibit little decay in peak amplitude from NW1 to NW49 (inset, Fig. 4B), which is consistent with the active propagation process. We fabricated structures containing 150 devices with an inter-device distance of only 400 nm and also successfully used this as a platform for directed neuronal growth (fig. S9).

We believe that the demonstration of large-scale integration of reproducible functional hybrid NW-neuron junctions has a variety of applications. These local NW-neurite junctions enable diverse and controllable multisite inputs while simultaneously mapping signal flow with high spatial and temporal resolution. These capabilities could be used to investigate multiple NW inputs and outputs to a single soma and to study synaptic processing in neural networks (*38*, *39*) with NW-neurite junctions used to reversibly inhibit or stop signal propagation along specific pathways while simultaneously mapping signal flow in dendrites and axons in the network. Second, the demonstrated reproducibility of the NW-cell devices and ability to integrate these hybrid structures on chips in a multicell array format has implications for developing flexible real-time cellular assays, for example, for drug discovery and testing. Last, the NW-neurite junctions can be applied to hybrid circuits where one might integrate different signals with a neuron and subsequently explore nanoelectronic circuit responses, as well as interfaces to implanted devices.

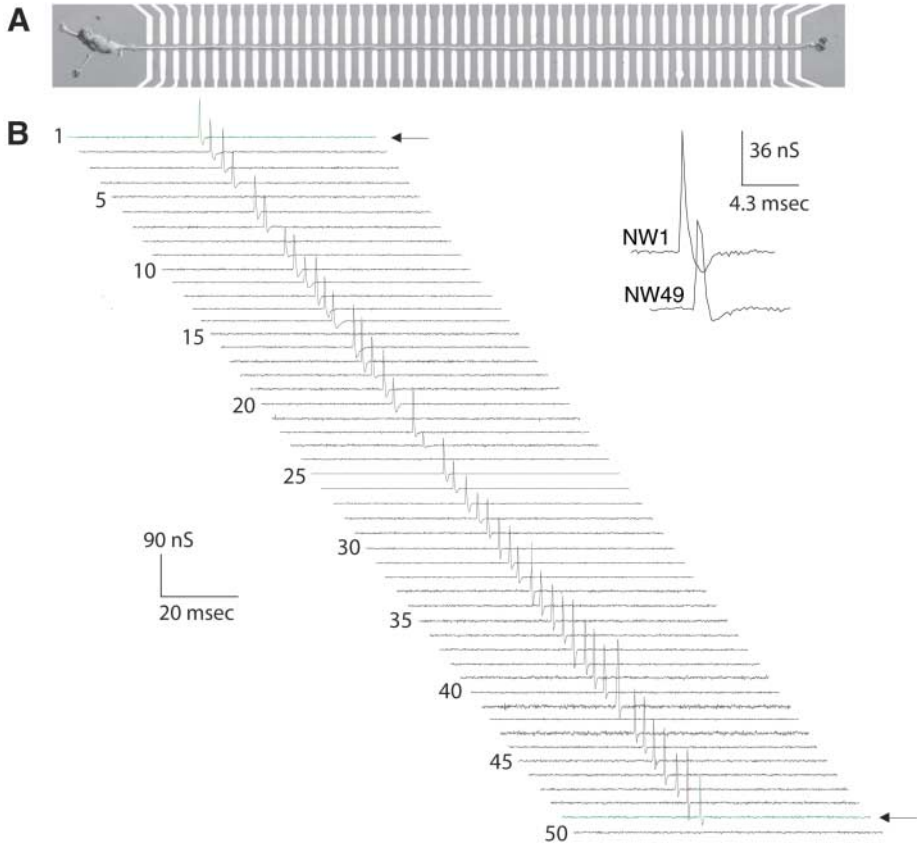

Fig. 4. Highly integrated NW-neuron devices. (**A**) Optical image of aligned axon crossing an array of 50 NW devices with a 10-μm interdevice spacing. (**B**) Electrical data from the 50-device array shown above. The yield of functional devices is 86%. The peak latency from NW1 (top arrow) to NW49 (bottom arrow) was 1060 μs.

References and Notes

1. A. R. Martin, B. G. Wallace, P. A. Fuchs, J. G. Nicholls, *From Neuron to Brain: A Cellular and Molecular Approach to the Function of the Nervous System* (Sinauer Associates Inc., Sunderland, MA, 2001).
2. U. Windhorst, H. Johansson, *Modern Techniques in Neuroscience Research: Electrical Activity of Individual Neurons in Situ: Extra- and Intracellular* (Springer, New York, 1999).
3. S. Marom, G. Shahaf, *Q. Rev. Biophys.* **35**, 63 (2002).
4. W. L. C. Rutten, *Annu. Rev. Biomed. Eng.* **4**, 407 (2002).
5. P. Fromherz, *ChemPhysChem* **3**, 276 (2002).
6. H. Oviedo, A. D. Reyes, *J. Neurosci.* **25**, 4985 (2005).
7. R. C. Froemke, M. M. Poo, Y. Dan, *Nature* **434**, 221 (2005).
8. G. J. Stuart, M. Hausser, *Nat. Neurosci.* **4**, 63 (2001).
9. A. Lambacher *et al.*, *Appl. Phys. A* **79**, 1607 (2004).
10. A. Offenhausser, C. Sprossler, M. Matsuzawa, W. Knoll, *Biosens. Bioelectron.* **12**, 819 (1997).
11. M. Merz, P. Fromherz, *Adv. Funct. Mater.* **15**, 739 (2005).
12. M. Voelker, P. Fromherz, *Small* **1**, 206 (2005).
13. C. D. James *et al.*, *IEEE Trans. Biomed. Eng.* **51**, 1640 (2004).

14. Y. Jimbo, N. Kasai, K. Torimitsu, T. Tateno, H. P. C. Robinson, *IEEE Trans. Biomed. Eng.* **50**, 241 (2003).
15. Y. Huang, C. M. Lieber, *Pure Appl. Chem.* **76**, 2051 (2004).
16. F. Patolsky, G. Zheng, C. M. Lieber, *Anal. Chem.* **78**, 4261 (2006).
17. Y. Cui, Q. Q. Wei, H. Park, C. M. Lieber, *Science* **293**, 1289 (2001).
18. G. F. Zheng, F. Patolsky, Y. Cui, W. U. Wang, C. M. Lieber, *Nat. Biotechnol.* **23**, 1294 (2005).
19. F. Patolsky *et al.*, *Proc. Natl. Acad. Sci. U.S.A.* **101**, 14017 (2004).
20. Y. Cui, Z. Zhong, D. Wang, W. U. Wang, C. M. Lieber, *Nano Lett.* **3**, 149 (2003).
21. G. F. Zheng, W. Lu, S. Jin, C. M. Lieber, *Adv. Mater.* **16**, 1890 (2004).
22. S. Jin *et al.*, *Nano Lett.* **4**, 915 (2004).
23. C. Wyart *et al.*, *J. Neurosci. Methods* **117**, 123 (2002).
24. C. D. James *et al.*, *IEEE Trans. Biomed. Eng.* **47**, 17 (2000).
25. Materials and methods are available as supporting material on *Science* Online.
26. S. M. Sze, in *Physics of Semiconductor Devices* (Wiley, New York, 1981), pp. 431–456.
27. A. T. Gulledge, G. J. Stuart, *J. Neurosci.* **23**, 11363 (2003).
28. M. Tarek, *Biophys. J.* **88**, 4045 (2005).
29. M. E. Larkum, J. J. Zhu, *J. Neurosci.* **22**, 6991 (2002).
30. R. Larry *et al.*, in *Fundamental Neuroscience* (Elseiver Science, San Diego, CA, 2003), pp. 115–136.
31. A. L. Hodgkin, A. F. Huxley, *J. Physiol.* **117**, 500 (1952).
32. L. G. Nowak, J. Bullier, *Exp. Brain Res.* **118**, 477 (1998).
33. R. Yuste, D. W. Tank, D. Kleinfeld, *Cereb. Cortex* **7**, 546 (1997).
34. S. Antic, G. Major, D. Zecevic, *J. Neurophysiol.* **82**, 1615 (1999).
35. H. Kawaguchi, K. Fukunishi, *Exp. Brain Res.* **122**, 378 (1998).
36. N. J. M. Rijkhoff, E. L. Koldewijn, P. E. V. van Kerrebroeck, F. M. J. Debruyne, H. Wijkstra, *IEEE Trans. Biomed. Eng.* **41**, 413 (1994).
37. A. Vuckovic, J. J. Struijk, N. J. M. Rijkhoff, *Med. Biol. Eng. Comput.* **43**, 365 (2005).
38. G. Q. Bi, M. M. Poo, *Nature* **401**, 792 (1999).
39. A. Frick, J. Magee, D. Johnston, *Nat. Neurosci.* **7**, 126 (2004).
40. B.P.T. thanks the NSF for graduate fellowship support. C.M.L. acknowledges support of this work by Defense Advanced Research Projects Agency and Applied Biosystems.

Supporting Online Material
www.sciencemag.org/cgi/content/full/313/5790/1100/DC1
Materials and Methods
SOM Text
Figs. S1 to S10
References

12 April 2006; accepted 18 July 2006
10.1126/science.1128640

Discrete Sandwich Compounds of Monolayer Palladium Sheets

Tetsuro Murahashi,[1]* Mayu Fujimoto,[1] Masa-aki Oka,[1] Yasuhiro Hashimoto,[1] Tomohito Uemura,[1] Yasuki Tatsumi,[1] Yoshihide Nakao,[2] Atsushi Ikeda,[2] Shigeyoshi Sakaki,[2] Hideo Kurosawa[1]*

Despite the abundance of "sandwich" complexes, in which two cyclic aromatic hydrocarbon ligands flank a metal center, this motif has not been extended to sheets of multiple metal atoms. We prepared and isolated two such compounds. In the first, three palladium centers form a planar triangular array, capped by chlorides, between two cycloheptatrienyl ligands. In the second, a pentapalladium sheet adopts an edge-sharing triangle-trapezoid skeleton between two naphthacene rings. The compounds were characterized by x-ray crystallography and nuclear magnetic resonance spectroscopy. The nature of bonding in the clusters was analyzed by quantum calculations.

The chemistry of metal sandwich complexes has developed intensively since the structure of ferrocene $(C_5H_5)_2Fe$ was elucidated in 1952 (*1*, *2*). The motif now plays an important role in catalysis and materials sciences (*3*, *4*). Most of the discrete sandwich complexes possess a mononuclear metal center between two small aromatic carbocyclic ligands, such as cyclopentadienyl or benzene (Fig. 1A). In contrast, compounds in which the carbon rings flank a monolayer of multiple metal atoms have not been isolated as discrete molecules, despite the fascinating implications of such layered sheet structure (Fig. 1B). The potential existence of these compounds was implicated by early observation of facial coordination of cyclopentadienyl or benzene ligands to triangular trimetal cores in a half-sandwich manner (*5*, *6*). More recently, a $Ni_3(benzene)_2$ species was detected through mass spectroscopy in a mixture of $Ni_n(benzene)_m$ clusters generated in the gas phase by laser vaporization (*7*). Stable structures of discrete metal monolayer sandwich compounds have also been discussed in theoretical studies (*8*). Moreover, formation of metal nanosheets between graphene layers has been observed through transmission electron microscopy (TEM) (*9*, *10*), which further stimulates the search for this (carbon sheet)−(metal sheet)−(carbon sheet) interaction in discrete molecules.

We sought to prepare palladium compounds that adopt this layered motif. Palladium is one of the most versatile transition metal catalysts for transformation of organic and inorganic substrates (*11*). Although mononuclear biscyclopentadienyl- and bisbenzene palladium complexes are unknown, polyatomic palladium frameworks seemed likely to form stably between extended unsaturated hydrocarbon ligands, in view of the isolation of bisbenzene dipalladium complexes (*12*, *13*) as well as the efficient formation of Pd sandwich chain compounds (*14*, *15*). Here, we report the successful isolation and structural characterization of two discrete metal monolayer sandwich compounds: $[Pd_3(C_7H_7)_2Cl_3][PPh_4]$ (**1**) and $[Pd_5(naphthacene)_2(toluene)][B(Ar_f)_4]_2$ (**4-toluene**), where $B(Ar_f)_4 = B[3,5\text{-}(CF_3)_2C_6H_3]_4$.

The cycloheptatrienyl (Tr) cation $[C_7H_7]^+$ has been widely studied as a transition metal ligand (*16*–*18*) but has rarely been used in palladium chemistry (*19*, *20*). Surprisingly, the reaction of $[Pd_2(dba)_3]$ (dba = 1,5-diphenyl-1,4-pentadien-3-one) and $[C_7H_7][BF_4]$ in the presence of $[PPh_4]Cl$ in CD_2Cl_2 afforded the biscycloheptatrienyl tripalladium complex $[Pd_3Tr_2Cl_3][PPh_4]$ (**1**) almost quantitatively after 10 min (Fig. 2A). The product **1** was isolated as wine-red microcrystals in 72% yield after recrystallization from hot acetonitrile. The structure of **1** was determined by x-ray diffraction analysis (Fig. 2B). The triangular tripalladium core is sandwiched between two planar cycloheptatrienyl ligands. The Pd−Pd bonds (2.745 to 2.789 Å) are within the range of normal Pd−Pd bond length (*21*). The two cycloheptatrienyl rings are slightly deviated from the mutually eclipsed position. Of the seven carbons in each ring, two pairs, C1-C2 and C3-C4 or C10-C11 and C12-C13, are located within the bonding distance (2.15 to 2.28 Å) from Pd1 and Pd2 or Pd2 and Pd3, respectively. The remaining carbon sets, [C5, C6, C7] or [C8, C9, C14], are bound rather irregularly to Pd3 or Pd1, respectively, with the shorter Pd3−C6 and Pd1−C8 lengths and the longer Pd3−C5, Pd3−C7, Pd1−C9, and Pd1−C14 lengths. The C−C bond lengths of

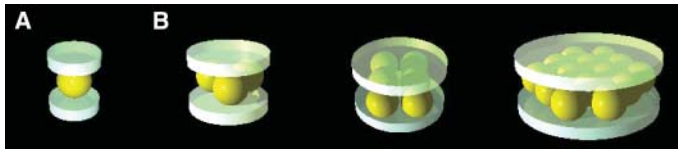

Fig. 1. Illustrated models of (**A**) metallocene and (**B**) hypothetical metal monolayer sandwich compounds.

[1]Department of Applied Chemistry, Graduate School of Engineering, Osaka University, and PRESTO, Japan Science and Technology Agency (JST), Suita, Osaka 565-0871, Japan. [2]Department of Molecular Engineering, Graduate School of Engineering, Kyoto University, Nishikyo-ku, Kyoto 615-8510, Japan.

*To whom correspondence should be addressed. E-mail: tetsu@chem.eng.osaka-u.ac.jp (T.M.); kurosawa@chem.eng.osaka-u.ac.jp (H.K.)